



Citation for published version:

Turner, J, Lay, E, Jungwirth, U, Varenko, V, Gill, HS, Estrela, P & Leese, H 2023, '3D-Printed Hollow Microneedle-Lateral Flow Devices for Rapid Blood-Free Detection of C-Reactive Protein and Procalcitonin', *Advanced Materials Technologies*, vol. 8, no. 16, 2300259. <https://doi.org/10.1002/admt.202300259>

DOI:

[10.1002/admt.202300259](https://doi.org/10.1002/admt.202300259)

Publication date:

2023

Document Version

Publisher's PDF, also known as Version of record

[Link to publication](#)

Publisher Rights

CC BY

University of Bath

Alternative formats

If you require this document in an alternative format, please contact:
openaccess@bath.ac.uk

General rights

Copyright and moral rights for the publications made accessible in the public portal are retained by the authors and/or other copyright owners and it is a condition of accessing publications that users recognise and abide by the legal requirements associated with these rights.

Take down policy

If you believe that this document breaches copyright please contact us providing details, and we will remove access to the work immediately and investigate your claim.

3D-Printed Hollow Microneedle-Lateral Flow Devices for Rapid Blood-Free Detection of C-Reactive Protein and Procalcitonin

Joseph G. Turner, Emily Lay, Ute Jungwirth, Valentyna Varenko, Harinderjit S. Gill, Pedro Estrela, and Hannah S. Leese*

Hollow microneedle devices as a technology for interstitial fluid extraction show promise for the minimally invasive point-of-care detection of analytes. Despite increasing efforts toward on-patch diagnostics, the use of hollow microneedles has been limited due to the complexity caused by integrating hollow microneedles with established point-of-care diagnostic techniques. Herein, a 3D printing method is utilized, to provide low-cost manufacturing of custom-designed hollow microneedle devices, allowing for easy integration with lateral flow assays for rapid and blood-free diagnostics. Microneedle surface modification through PEGylation results in prolonged and enhanced hydrophilicity, enabling passive uptake of small volume samples ($\approx 22.5 \mu\text{L}$) and an enhanced shelf life. The hollow microneedle devices are deemed non-cytotoxic to cell types found within the skin following short-term and prolonged exposure in accordance with ISO10993. Furthermore, the devices demonstrate high mechanical strength and successfully penetrate porcine skin grafts without damaging the surrounding skin morphology. This work also demonstrates for the first time the use of hollow microneedles for the simultaneous detection, at clinically relevant concentrations, of C-reactive protein ($\text{LoD} = 10 \mu\text{g mL}^{-1}$) and procalcitonin ($\text{LoD} = 1 \text{ ng mL}^{-1}$), through porcine skin, ultimately demonstrating the beneficial use of manufactured 3D-printed hollow microneedles towards low-cost blood-free diagnostics of inflammation markers.

1. Introduction

Diagnosis is an essential part of health-care. Although clinical laboratories offer sensitive, specific assays, such as blood culture and high-throughput immunoassays for infection, they are often time and labor intensive, costly, and dependent on well-trained operators, which can result in reduced access in limited resource settings.^[1,2] Sampling adequate volumes of blood for lab based diagnostics is also problematic, causing issues such as requiring medical professionals, additional handling, risk of accidental transmission, as well as being invasive to the patient, and the potential for subsequent infection.^[3,4] In contrast, rapid diagnostic tests, such as lateral flow assays (LFAs) are inexpensive, readily available, and do not require blood samples, enabling informed treatments agnostic to settings and environmental factors making them suitable for diagnostic use in limited resource settings.^[5,6]

J. G. Turner, H. S. Leese
Materials for Health Lab
Department of Chemical Engineering
University of Bath
Bath BA2 7AY, UK
E-mail: h.s.leese@bath.ac.uk


J. G. Turner, H. S. Gill, P. Estrela, H. S. Leese
Centre for Bioengineering and Biomedical Technologies (CBio)
University of Bath
Bath BA2 7AY, UK

E. Lay, U. Jungwirth, V. Varenko
Department of Life Sciences
University of Bath
Bath BA2 7AY, UK

E. Lay, U. Jungwirth, H. S. Gill
Centre for Therapeutic Innovation
University of Bath
Bath BA2 7AY, UK

H. S. Gill
Department of Mechanical Engineering
University of Bath
Bath BA2 7AY, UK

P. Estrela
Department of Electronic and Electrical Engineering
University of Bath
Bath BA2 7AY, UK

 The ORCID identification number(s) for the author(s) of this article can be found under <https://doi.org/10.1002/admt.202300259>

© 2023 The Authors. Advanced Materials Technologies published by Wiley-VCH GmbH. This is an open access article under the terms of the Creative Commons Attribution License, which permits use, distribution and reproduction in any medium, provided the original work is properly cited.

DOI: 10.1002/admt.202300259

Following the onset of a bacterial infection, the body naturally responds by increasing local blood flow (causing inflammation) and directing cells from the immune system to produce antibodies to attack foreign bacteria.^[7] During this, certain proteins are released into the bloodstream, making them useful as systemic inflammatory markers for diagnosis.^[8] In clinical practice, elevated C-reactive protein (CRP) and procalcitonin (PCT) levels are nonspecific but are commonly measured to help identify an inflammatory response due to conditions such as: myocardial infarction, pneumonia and sepsis.^[9–12] Sepsis is a life-threatening extreme inflammatory response, most commonly linked to bacterial infections. Worldwide, sepsis is the cause of 11 million deaths each year,^[13] with ≈ 20 million sepsis cases in low- and middle-income countries,^[14] with neonatal sepsis accounting for over 3 million cases.^[15] The key for treating sepsis is quick diagnosis, but the complex inflammatory response sequence makes diagnosis challenging since there is not a sufficient single biomarker concentration for a prolonged time that can be directly linked to sepsis, making multiple biomarker diagnostics appropriate.^[16] In some cases, CRP provides prognostic value, since concentrations fall quickly once the cause of inflammation has been resolved, making it useful for monitoring disease activity and response to treatment.^[17,18]

Interstitial fluid (ISF) is a highly accessible alternative source of biomarkers found in skin and has a high degree of correlation with blood for many inflammation markers of interest making it useful for blood-free diagnostics.^[19,20] Hollow microneedles (HMNs) contain a hollow bore, that enable access to ISF, providing the capability of transporting drugs through the interior by diffusion or pressure-driven flow,^[21] and extraction of ISF through suction or capillary action.^[22,23] Since the first appearance in a 1971 patent,^[24] hollow microneedle research has primarily focused on transdermal drug delivery.^[21] In 2005, the first report of glass based hollow microneedles for ISF extraction through a vacuum pump (and subsequent monitoring of glucose levels) was reported.^[25] Typically analysis of collected ISF is performed off-line with samples stored, transported, and tested using alternative techniques,^[22] increasing time and cost associated with diagnosis. On-patch diagnostics are highly beneficial, removing problems associated with off-line detection, however, is limited through integration of hollow microneedles with existing analytical techniques. Adding to the need for intense research toward a low-cost on-patch point of care diagnostic device, first reported using hollow microneedles in 2020.^[26]

Conventional methods of hollow microneedle fabrication, such as deep reactive ion etching and microhole drilling,^[27,28] are time consuming and require the use of expensive specialized equipment. 3D printing is an attractive alternative allowing for easier customization and intricate microneedle architectures otherwise difficult to achieve with alternative industrial-scale methods. Low-force stereolithography (SLA) 3D printing is a desktop technique useful for low-cost manufacturing but is limited by the resolution, restricting designs to microscale 3D printing. Nanoscale 3D printing techniques, such as two-photon polymerization (2PP), generate nanoscale structures but come with a high cost, making it more challenging for mass manufacturing or widescale use. SLA 3D printing provides a suitable balance between manufacturing cost and hollow microneedle per-

formance, first described in 2019.^[29] Despite SLA being advantageous for development of hollow microneedle devices, their translation to medical device use must be assessed in accordance with *ISO 10993: Biological evaluation of medical devices*, with cytotoxicity, sensitization, and irritancy to cells the main points to address.^[30] To date, minimal research has assessed the effect of commercially available resins on relevant skin cell types such as keratinocytes, and fibroblast cells, with one example using cardiac muscle cells.^[31]

Here we report, for the first-time, low-cost SLA 3D-printed hollow microneedle-based sensing devices for, easy-to-use, blood-free detection of desirable biomarkers. This unique design allows for the integration of hollow microneedles with LFAs (HMNs-LFA) enabling rapid detection of CRP and PCT in sample fluids. We demonstrate sufficient mechanical strength and ability to penetrate *ex vivo* porcine skin without damage to the microneedles or surrounding skin. We demonstrate the ability to penetrate porcine skin and passively extract and guide fluid samples onto the sample pad of LFAs without the use of any external pumps. Increased and sustained fluid flow through the device was achieved through surface functionalization, and we demonstrate successful simultaneous detection of CRP and PCT, as low as $10 \mu\text{g mL}^{-1}$ and 1 ng mL^{-1} , respectively, within spiked buffer solutions. In accordance with ISO 10993, we demonstrate the hollow microneedle devices biocompatibility with keratinocytes and fibroblast cells. Ultimately demonstrating a tailororable low-cost, point-of-care device for blood-free diagnostics.

2. Results and Discussion

2.1. Fabrication of Hollow Microneedle-Lateral Flow Assay Devices

Hollow microneedle devices were successfully printed using SLA 3D printing. High Temp resin is a specialized commercially available resin compatible with SLA 3D printers with the ability to withstand increased temperatures and pressures compared to standard resins. UV/Heat post-processing also increases heat deflection temperature, mechanical strength, and parts durability.^[32] These enhanced properties make the High Temp resin highly suitable for direct fabrication of hollow microneedles since various sterilization techniques have little chemical or structural impact on the produced hollow microneedles. TGA analysis showed an initial mass decrease at $\approx 275 \text{ }^\circ\text{C}$ and maximum derivative at $420 \text{ }^\circ\text{C}$ (Figure S1, Supporting Information).

The hollow microneedle devices consist of 15 tear-drop shaped hollow microneedles (5×3) on top of a large base with a 1.5 mm slit for insertion of LFAs (Figure 1). Increasing the printing tilt angle, results in a sharper tip for microneedles. Printing the hollow microneedles at a 45° tilt with the needles *parallel* to the printer edge resulted in an optimum tip diameter while maintaining print accuracy (printed at 45° *perpendicular* to the printer edge caused the bore to be fully sealed by excess resin during printing, Figure S2, Supporting Information). The resultant hollow microneedles have a height of $\approx 998.5 \pm 2.6 \mu\text{m}$, bore size $495.6 \pm 4.3 \mu\text{m}$, and tip radius of $24.9 \pm 2.6 \mu\text{m}$ highlighting accuracy and reproducibility of the 3D printer. The tear-drop shape was used to compromise between tip diameter with bore quality. It was found that a bore diameter below $500 \mu\text{m}$ risked bore

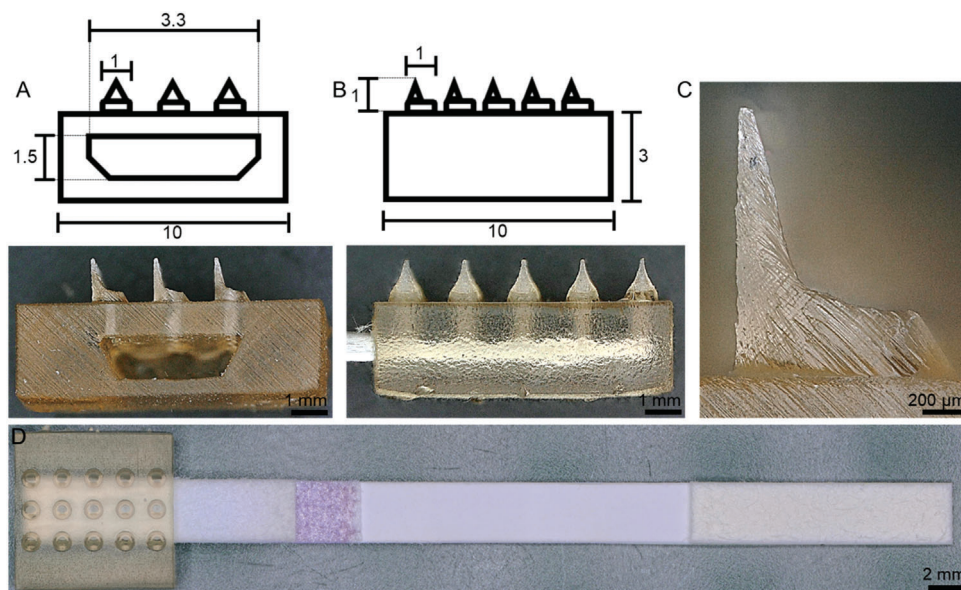


Figure 1. Hollow microneedle-lateral flow assay device. Schematic (dimensions in mm) and optical images of A) front profile with 1.5 mm slit and B) side profile of the device. C) Close-up optical image of a single hollow microneedle. D) Optical image of complete hollow microneedle-lateral flow assay for CRP diagnostics.

blockage during printing as a result of the printer resolution, restricting the use of typical cone/pyramid-based needles of the same overall dimensions.

It has been reported that increasing the length of the microneedle results in increased pain during application, due to interactions with pain receptors:^[20] a needle length of 480 μm induces a pain response of only 5% of that for a hypodermic needle, while increasing the length to 1450 μm increases the response to 37%.^[33] As a result, the needle height used (1000 μm) allows for a balance between sufficient penetration depth for ISF extraction and patient comfort in application. It has been reported that hollow microneedles, of similar dimensions, can extract $\approx 1.5\text{--}4\ \mu\text{L}$ needle⁻¹ of ISF in 5 min.^[22,26] Resulting in 15 hollow microneedles able to extract an approximately 22.5–60 μL in 5 min, which is sufficient for the LFA to function correctly (experimentally observed as a minimum of 20 μL).

3D printing provides increased flexibility for microneedle fabrication often restricted by traditional fabrication techniques. Design alternations can be performed through CAD and quickly implemented for use. Altering the number of needles on the array will affect the total volume of extracted ISF, and 3D printing allows for quick alteration and optimization depending on the sample volume required for reliable diagnosis.^[22,26] The 3D printer utilizes a small resin volume per hollow microneedle array ($\approx 0.2\ \text{mL array}^{-1}$) and has a relatively large build platform and fast production speed, resulting in a viable method of low-cost mass manufacturing of hollow microneedles. Quantitatively, it is estimated a maximum of 170 devices could be printed at one time on the build platform, with sufficient spacing surrounding the parts, using $\approx 34\ \text{mL}$ of resin, taking $\approx 3\ \text{h}$ at the highest resolution, and costing $\approx \$7.40$ USD in total, equating to $\approx 0.04\text{¢}$ per hollow microneedle array.

2.2. PEGylation Surface Modification

To ensure continuous and enhanced fluid flow through the hollow microneedles, it was necessary to modify the hollow microneedles with a long-lasting hydrophilic coating (PEGylation).^[34] Without PEGylation, fluid would not flow through the needles due to the water surface tension around the needles caused by the hydrophobicity of the 3D-printed material. Hollow microneedles with a water contact angle (WCA) $< 61^\circ$ was observed to have enhanced water fluid flow with a WCA $> 61^\circ$ hindering water uptake. The untreated hollow microneedle (untreated-HMNs) surface is hydrophobic with no change over time, with an average WCA of $101 \pm 1^\circ$ ($n = 18$) (Figure 2A), similar to that observed by Bacha et al.^[35] In application, no fluid was able to flow through the needles of untreated hollow microneedles, highlighting the need for surface modification.

The Young-Laplace equation (Equation 1) can be used to model the capillary pressure difference (ΔP) sustained within a single hollow microneedle, due to water surface tension (γ , $72.0\ \text{mN m}^{-1}$)

$$\Delta P = \frac{2\gamma \cos(\theta)}{a} \quad (1)$$

where a is the radius of the hollow microneedle bore (250.0 μm) and θ is the WCA ($^\circ$). To maintain hydrostatic equilibrium, the capillary pressure is balanced by the change in height of the fluid within the hollow microneedle (h) (Equation 2)

$$h = \frac{2\gamma \cos(\theta)}{\rho g a} \quad (2)$$

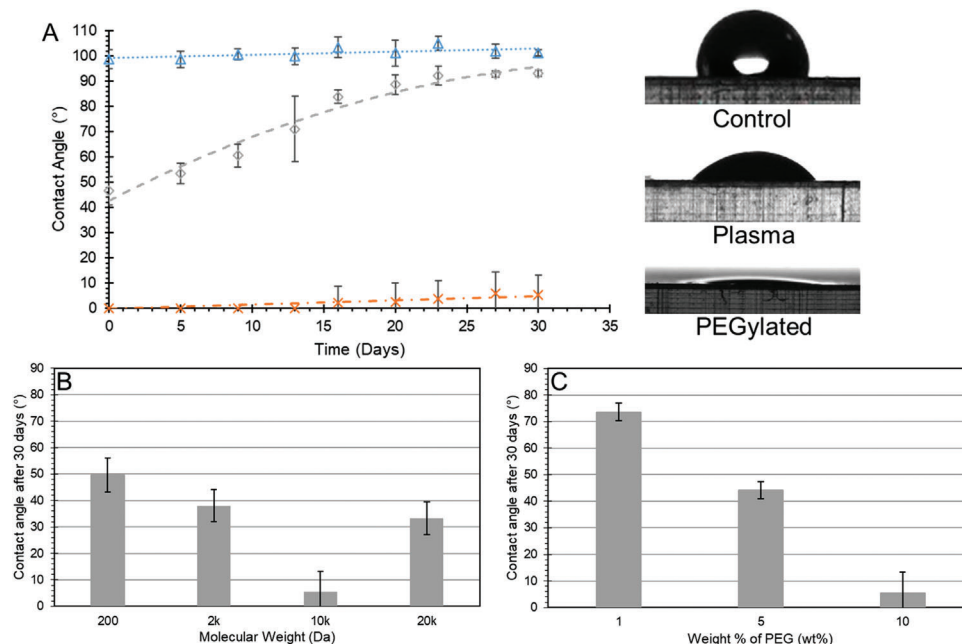


Figure 2. PEGylation characterization. A) Wettability over time with corresponding water droplet profile for untreated (blue triangle), plasma treated (gray circle) and PEGylated (orange cross), $n = 9$. B) Varying molecular weight of PEG used, $n = 9$ and C) varying weight % of PEG in solution, $n = 9$.

where ρ is the density of the fluid (997.0 kg m^{-3}) and g is the gravitational constant (9.8 m s^{-2}). For the untreated hollow microneedles (WCA = $101 \pm 1^\circ$), the hydrophilic nature results in a capillary pressure of -5.1 Pa , resulting in a height of -0.5 mm which supports the observed lack of fluid flow through the untreated hollow microneedles in application.

Following plasma treatment, the activated surface becomes hydrophilic with an initial reduction in WCA to $48 \pm 6^\circ$ ($n = 18$) after sterilization (Figure 2A). Following UV/heat treatment, the 3D prints primarily consist of crosslinked poly(methacrylic acid) (PMAA) with methyl ($-\text{CH}_3$) and carboxylic acid groups ($-\text{COOH}$) found on the surface. Following plasma treatment, surface energy increases and surface methyl groups are replaced by alcohol ($-\text{OH}$) groups, which are more hydrophilic in nature and account for the increase in surface hydrophilicity. However, over time hydrophobic recovery (migration of low M_w species from the surface^[36]) results in an increase of WCA to $\approx 61 \pm 5^\circ$ ($n = 18$) after 10 days, a significant increase ($p < 0.001$). In application, freshly plasma treated samples had increased fluid flow through the needles, however after 10 days fluid flow was hindered and no longer aided by the surface hydrophilicity. Freshly plasma treated samples (WCA = $48 \pm 6^\circ$) have a capillary pressure of 20.8 Pa and height of 2.0 mm , which is greater than the 1.5 mm distance between the opening of the bore and the sample pad located within the HMN-LFA. However, after 10 days (WCA = $61 \pm 5^\circ$), the pressure reduces to $\approx 14.7 \text{ Pa}$ and height of $\approx 1.5 \text{ mm}$, which is equal to the 1.5 mm distance and highlights how the fluid flow becomes hindered when the contact angle rises above 61° .

Following the PEGylation process, the surface becomes very hydrophilic, recording a nonmeasurable WCA (0°) (Figure 2A). Once submerged in a PEG solution, PEG can form hydrogen bonds between surface carboxylic acid groups ($-\text{COOH}$) and

ethylene glycol groups in PEG,^[37] aided by the high surface energy (Figure S3, Supporting Information). Following 30 days, surface hydrophilicity remained unaltered and the WCA rose slightly to $\approx 5^\circ$ but the surface remained very hydrophilic. The initial PEGylated hollow microneedle samples (WCA = 0°) have a capillary pressure of 29.3 Pa and height of 3.0 mm , far greater than the 1.5 mm distance between the bore opening of the microneedle and sample pad. In application, enhanced fluid flow was still observed after 30 days, highlighting a long-lasting hydrophilic coating (WCA = 5°). This sustained hydrophilicity over time gives confidence to a permanent coating, allowing for storage of samples for later use.

The M_w of PEG used during PEGylation affected the longevity of the resultant wettability, with the concentration maintained at $10 \text{ wt}\%$ (Figure S4A, Supporting Information). In all cases directly after PEGylation, the PEGylated hollow microneedles had a nonmeasurable WCA due to the extreme hydrophilicity of the surface. After 30 days, on increasing the M_w of PEG, the WCA decreased from $50 \pm 6^\circ$ (200 Da) to 5° (10 kDa) ($n = 9$, $p < 0.001$) respectively, likely due to hydrophobic recovery and coating inconsistencies for M_w 200 Da (Figure 2B). However, it was found that increasing the M_w to 20 kDa also had a negative impact on the longevity of the hydrophilic coating, recording a WCA of $33 \pm 6^\circ$ after 30 days, likely due to the solubility of the PEG in solution resulting in an inconsistent coating. As a result, 10 kDa was selected as an optimum M_w for coating the needles. Varying the weight percentage of PEG in solution also impacted the resultant longevity of the hydrophilic effect, with M_w maintained at 10 kDa (Figure S4B, Supporting Information). As expected, the higher PEG wt% formed a more consistent and continuous coating between the PEG and the hollow microneedle surface after 30 days (Figure 2C). 1 , 5 and $10 \text{ wt}\%$ resulted in a WCA of $74 \pm 3^\circ$, $44 \pm 3^\circ$, and 5° , respectively after 30 days, a significant

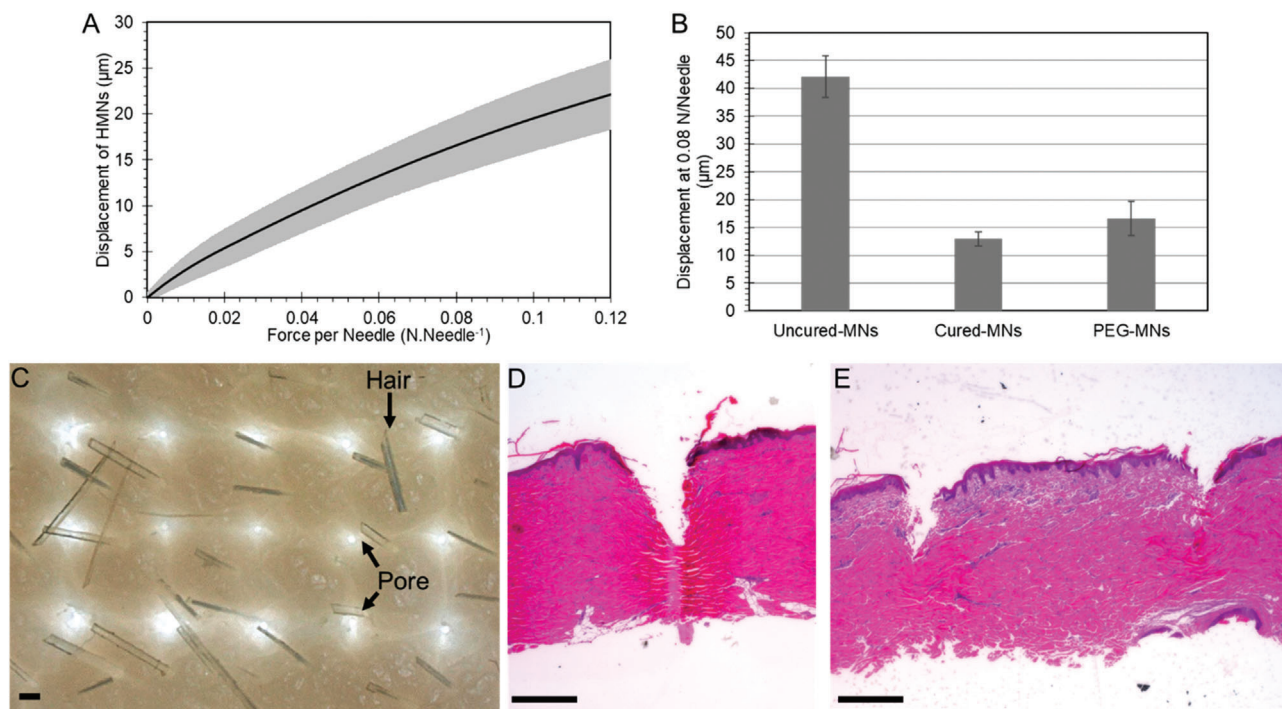


Figure 3. Mechanical properties and skin penetration of porcine skin. A) Resultant displacement with increasing force for PEGylated hollow MNs. B) Comparison of displacement at 0.08 N/Needle for uncured, cured, and PEGylated MNs. C) Porcine skin penetration after ≈ 1.5 N applied force. Cross section of the porcine skin after hematoxylin and eosin (H&E) staining showing pierced skin of D) a single and E) multiple needles in array. Scale bar equals 0.5 mm.

difference between 1 and 10 wt% ($n = 9$, $p < 0.001$). The work of adhesion (W_{sl}) changed with varying hydrophilicity over time for the samples (Figure S5, Supporting Information), showing that the adhesion energy between a solid and liquid surface can be increased by increasing the hydrophilicity of the solid surface.^[38]

Atomic force microscopy (AFM) determined the effect of post-treatment and surface modification on surface roughness across twenty, $10 \times 10 \mu\text{m}$ scan areas. Following plasma treatment, the surface roughness increased to 482.2 ± 51.4 nm, compared to 426.3 ± 33.6 nm for control samples ($p < 0.001$), caused by an etching effect occurring during plasma treatment.^[39] Following PEGylation, the surface roughness significantly reduced 272.3 ± 40.6 nm in comparison to the plasma treated samples ($p < 0.001$) (Figure S6, Supporting Information).

The exact chemical composition of the photocurable High Temp resin used is commercially confidential. However, The FTIR spectrum shares characteristic absorption peaks associated with methacrylate compounds (Figure S7, Supporting Information). The absorption bands at 1720 and 1695 cm^{-1} can be attributed by the C=O stretching of the carbonyl group. The acrylate's C-H and C=C stretch can be found at 1456 and 1383 cm^{-1} , respectively. C-O stretching, and C-C-O stretching can be found at 1250 and 1154 cm^{-1} respectively. The peaks at 955 , 810 , and 750 cm^{-1} can be attributed to CH_2 , C-O-C stretching and C-H, respectively. The effect of the PEGylation process on the molecular structure can be observed in FTIR traces, where newly formed -OH groups are shown by the broad peak at 3300 cm^{-1} and changes in the carboxylic acid occurring between 1700 and 1500 cm^{-1} .

2.3. Mechanical Properties and Porcine Skin Penetration

To characterize the intrinsic mechanical strength of the hollow microneedle arrays, a compressive force was applied, and resultant displacement recorded. It is widely reported that $0.08 \text{ N Needle}^{-1}$ is the minimum force required to penetrate human skin,^[40] meaning a minimum force of 1.2 N is required for this microneedle array design. After testing, the hollow microneedles did not exhibit any plastic deformation or failure following compression up to a total compressive force of 2 N , as highlighted by the nearly linear relationship between force and displacement (Figure 3A). The mechanical strength of the 3D-printed hollow microneedles were tested prior to UV/Heat treatment (uncured-HMNs), after full UV/heat treatment (cured-HMNs) and after PEGylation (PEG-HMNs) to monitor the effect of post-treatments on mechanical strength (Figure 3B). The uncured-HMNs recorded a $42.3 \pm 3.8 \mu\text{m}$ ($n = 3$) displacement ($4.2 \pm 0.4\%$ of initial height) at $0.08 \text{ N Needle}^{-1}$ with a Young's modulus calculated at 1.1 GPa . In comparison, at $0.08 \text{ N Needle}^{-1}$, the heat/UV treatment resulted in an increased mechanical strength with a displacement of $13.0 \pm 1.2 \mu\text{m}$ ($n = 3$, $1.3 \pm 0.1\%$ of initial height) and an increased Young's modulus (3.3 GPa). Following PEGylation mechanical strength marginally reduced to a displacement of $16.6 \pm 3.0 \mu\text{m}$ ($n = 3$, $1.7 \pm 0.3\%$ of initial height) and Young's modulus of 3.1 GPa . There was a significant difference between the displacement of the uncured-HMNs with both cured-HMNs ($p = 0.009$) and PEG-HMNs ($p = 0.003$) but a nonsignificant difference between the cured-HMNs and PEG-HMNs ($p = 0.16$). Highlighting the benefit of post UV/heat

treatment on mechanical strength. Despite the slight increase in displacement following PEGylation, the recorded displacement is nonsignificant in comparison to the initial height of the hollow microneedle devices (4 mm), and no visual damage occurred following compression. It has been reported that microneedles with an aspect ratio below 12:1 (length to diameter) should have a Young's modulus above 3 GPa to reduce risk of sudden failure and increase success of penetration,^[41] the cured-HMNs and PEG-HMNs have a calculated Young's modulus of 3.3 and 3.1 GPa, respectively. Giving confidence to sufficient mechanical strength to avoid damage in application. Further dynamic mechanical analysis (DMA) curves can be found in Figure S8 (Supporting Information).

The PEG-HMNs ability to penetrate skin was assessed using *ex vivo* porcine skin grafts. Porcine skin is a widely accepted model for human skin,^[42] as it presents a similar composition, with a stratum corneum thickness of 20–26 μm and an epidermis ranging from 30 to 140 μm compared to 50 to 120 μm for human skin.^[43] The PEG-HMNs were subjected to ≈ 1.5 N (150 g) applied directly onto the base of the hollow microneedles, exceeding the 1.2 N minimum force. The PEG-HMNs penetrated porcine skin successfully without damage to surrounding skin or the PEG-HMNs themselves. An under light was used to enhance the image and highlight resultant pores in porcine skin, showing 100% skin penetration of the PEG-HMNs (Figure 3C). Histological analysis was performed to evaluate the effects of microneedle penetration (via thumb press application) in skin tissue. The hollow microneedles pierce through the outer epidermis and into the dermis layer (Figure 3D,E). The depth cavity was calculated at $\approx 758 \pm 41$ μm ($n = 9$) long. In application, this would allow for collection of ISF located within the dermis while avoiding nerve endings located deeper within the skin. Images of unpierced skin prepared using the same method can be found in Figure S9 (Supporting Information). Ultimately, adding confidence that the hollow microneedle arrays can successfully penetrate through skin without damage.

To further assess mechanical properties into porcine skin, porcine skin was attached to the lower titanium plate of the DMA with PEG-HMNs attached to the upper plate and a compression applied as previous (Figure S10, Supporting Information). Following testing, the total recorded displacement was 446.3 ± 19.4 μm at 0.08 N Needle⁻¹ ($n = 3$). Assuming a 16.6 ± 3.0 μm displacement due to compression of the hollow microneedles, infers a 429.7 ± 19.6 μm displacement associated with the attached porcine skin (Figure S10, Supporting Information). This displacement measurement may not be a direct correlation to the microneedle penetration depth into the skin. To further investigate, linear-torsion dynamic tests were performed at various locations on a porcine skin sample. Hollow microneedles were brought into contact with the skin before starting the measurement with a target depth of 750 μm (Figure S11, Supporting Information). The initial increase in penetration depth (up to 641.3 ± 30.4 μm) uses a smaller force initially (≈ 3 N) (Figure S11C–E, Supporting Information). Over the 200 s measurement, the force profile indicates variability in the porcine skin in various places, with the range of force between 3.2 N up to a maximum force recorded at 4.7 N to reach 0.75 mm depth, equaling 0.2 to 0.3 N Needle⁻¹ $\approx 2.6\times$ greater than the 0.08 N Needle⁻¹ minimum force required. Regardless of the force required to penetrate and

subsequently go further into the skin, no damage to the hollow microneedles was observed and indicated that the devices can still penetrate skin when variable mechanical strength is required (i.e., variability in skin mechanics).

2.3.1. Biological Evaluation

ISO 10993 concerns the biological evaluation of medical devices, with ISO 10993-5 describing test methods to assess *in vitro* cytotoxicity, one of the main concerns for a medical device.^[30] High Temperature resin is not listed commercially as biocompatible, however possess physical and thermal properties that commercially available biocompatible resins do not have, making it highly suitable for hollow microneedle applications. Cytotoxicity testing concerns cell death and inhibition of colony formation caused by direct exposure to medical devices or an extract from the device.^[30] The latter assesses whether leachable substances could induce a cytotoxic effect.

Human dermal fibroblast cells (HuDAF) and human keratinocytes (Km) are the predominant cells found within the skin and are therefore used to test the impact of the devices on cell viability. According to ISO 10993, if cell viability exceeds 70% after the exposure to the device or extract, it is classed as nontoxic while a reduction of cell viability below 70% is classed as cytotoxic. Untreated cells were used as a negative control and acted as a baseline for comparison with results. Uncured resin was used as a positive control and significantly reduced the cell viability to $30.0 \pm 13.5\%$ and $36.7 \pm 18.6\%$ ($n = 3$) for HuDAF and Km cells, respectively (Figure 4A,B).

The biocompatibility of PEGylated devices was tested. PEG is commonly used as a biocompatible hydrophilic coating typically used in drug delivery.^[44] Indeed, the PEGylated devices barely reduced the cell viability of HuDAFs and Km cells ($85.7 \pm 5.2\%$ and $92.9 \pm 10.7\%$, approximately a 14% and 7% reduction, respectively) (Figure 4A,B). This nonsignificant reduction indicates nontoxicity of the PEGylated samples ($p < 0.001$). Furthermore, leaching of uncured monomers and other potential toxic substances from the devices was tested. The devices were incubated for 24 h in culture media (CM) and subsequently HuDAF and Km cells were exposed to the obtained CM. The cell viability of both cell models was again not reduced, with a cell viability of $85.9 \pm 1.3\%$ and $93.2 \pm 7.6\%$, respectively. Representative bright-field images of HuDAF show that only in samples exposed to the uncured samples cell death was observed (Figure 4C–F).

In addition to the PEGylated samples, plasma treated only samples were tested for improved biocompatibility of standard 3D-printed samples. HuDAF and Km cells in direct contact with plasma treated samples had a viability of $89.1 \pm 7.2\%$ and $91.4 \pm 8.8\%$, respectively (Figure S12, Supporting Information). HuDAF and Km cells exposed to CM from plasma treated samples had a viability of $100.3 \pm 9.8\%$ and $89.2 \pm 9.7\%$, respectively.

In addition to the cell viability assay, colony formation assays with breast tumor cells (BTCs) were performed (Figure S12, Supporting Information). Briefly, the colony forming capacity of BTCs was assessed after direct exposure to both plasma treated and PEGylated devices, exposure to CM and exposure to the uncured resin (Figure S12, Supporting Information). As expected, the uncured resin completely inhibited BTC colony formation,

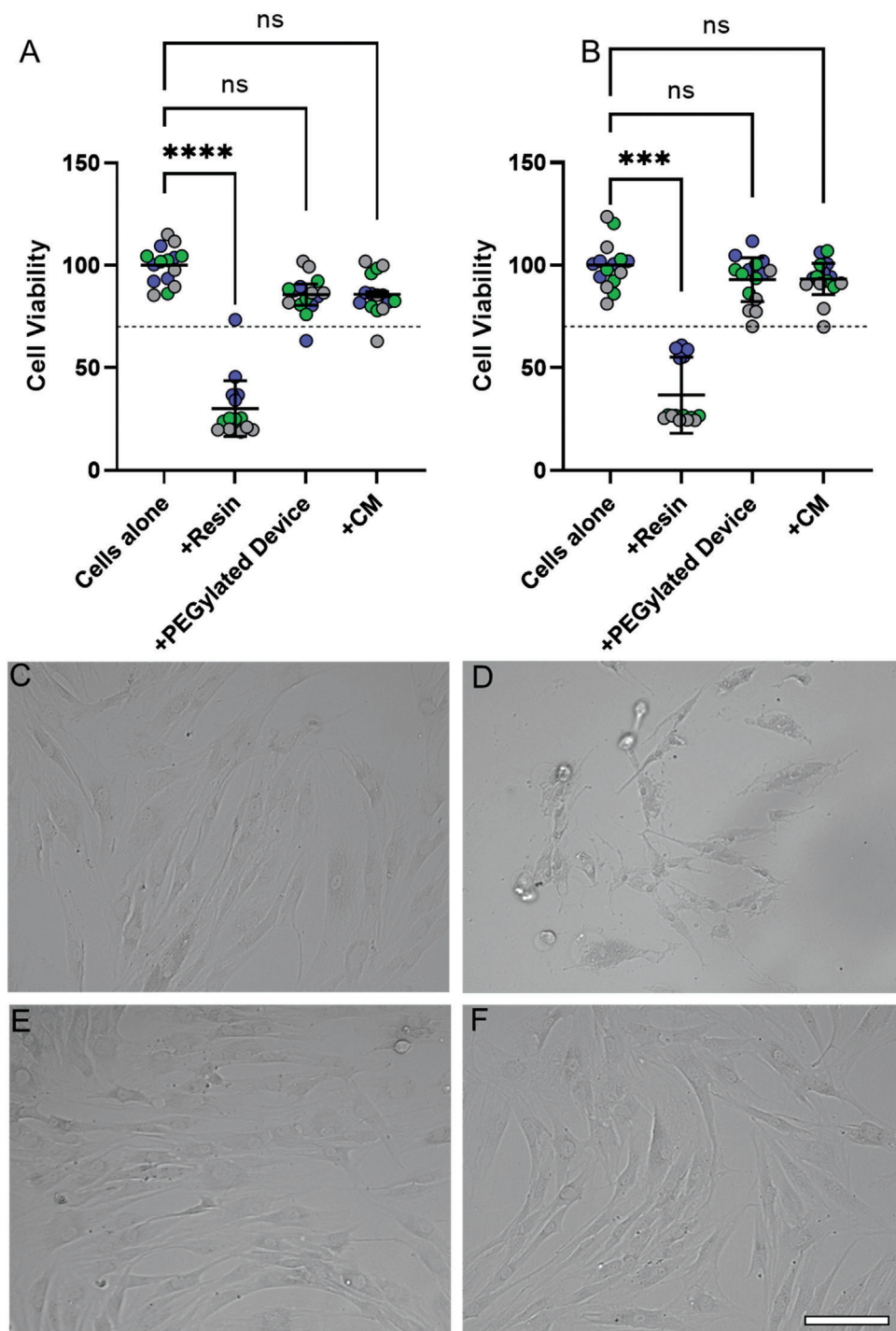


Figure 4. Biological evaluation of 3D-printed devices. Cell viability of A) human dermal fibroblast cells and B) human keratinocytes exposed to PEGylated samples, CM from the devices or uncured resin (resin) for 24 h. Shown are superplots of $n = 3$ individual experiments (mean \pm SD). Colors indicate the five replicas of each experiment. One-way ANOVA with Tukey's post hoc test, where n.s.; not significant ($p > 0.05$), *** $p < 0.001$ and **** $p < 0.0001$. The dashed line at 70% depicts the cytotoxic cut off, based on ISO 10993-05. Representative images of C) untreated HuDAFs or HuDADs following 24 h exposure to D) resin, E) PEGylated device or F) PEGylated device CM. Scale bar is 100 μm .

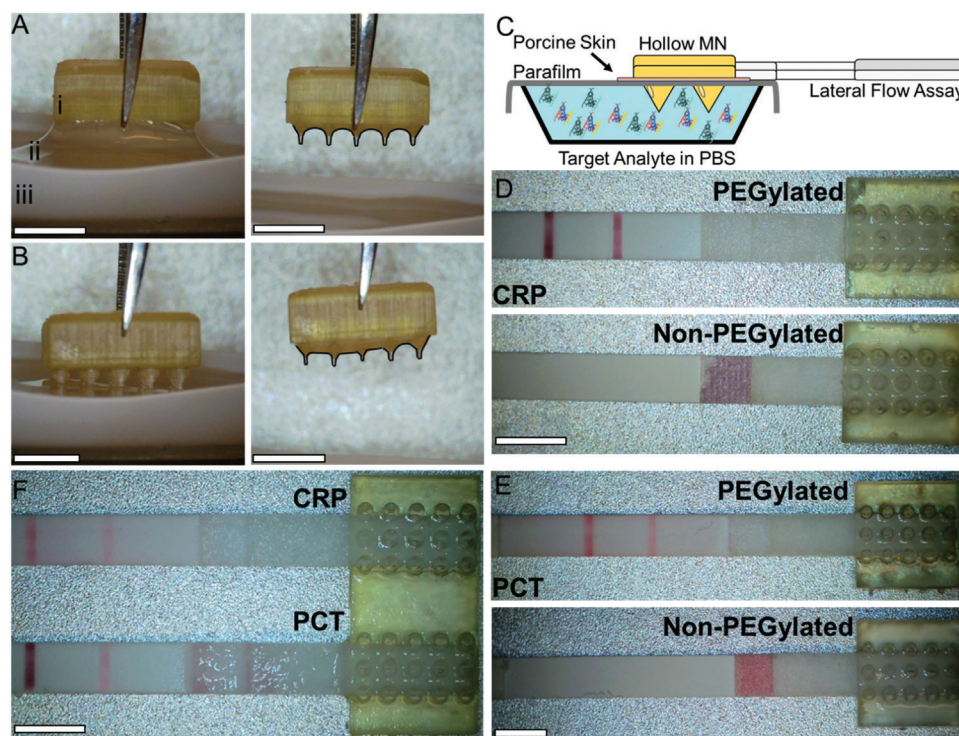


Figure 5. Fluid flow through hollow microneedles. Showing: A) PEGylated and B) untreated i) hollow microneedles (left) making initial contact to ii) spiked solution within iii) weighing boat and (right) being removed. PEGylated and untreated HMN-LFAs following 5 min in C) CRP and D) PCT solution. E) Simultaneous detection of CRP and PCT in spiked solutions. Scale bar equals 5 mm.

while both plasma treated devices and PEGylated devices had no significant impact on BTC colony formation.

Together, these results highlight an effective post-processing procedure to remove uncured toxic resin and ensured complete crosslinking of the samples. Both plasma-treated and PEGylated hollow microneedle devices have nontoxic properties. Despite not being listed as biocompatible, this current experimentation suggests PEG-HMNs are nontoxic, although further *in vivo* experimentation is still required to exclude sensitization and irritation.

2.4. 3D-Printed Hollow Microneedle-Lateral Flow Devices for Rapid Blood-Free Diagnostics

As discussed, hollow microneedles are reported to extract an approximate minimum volume of $1.5 \mu\text{L needle}^{-1}$ of ISF in $\approx 5 \text{ min}$,^[22,26] resulting in an estimated minimum total volume of $22.5 \mu\text{L}$ collected in 5 min. This volume was found to be sufficient for the fluid to flow up the HMNs and onto the LFA tests, where a minimum volume of $20 \mu\text{L}$ is required for the LFA to function correctly.

To demonstrate the incorporation of the HMN-LFA devices, commercially available CRP- and PCT-LFAs, with $10 \mu\text{g mL}^{-1}$ and 1 ng mL^{-1} limit of detection, respectively, were used with untreated (untreated-HMNs), plasma treated (plasma-HMNs) and PEGylated (PEG-HMNs) hollow microneedles. The hydrophilicity of the PEGylated hollow microneedles resulted in enhanced adhesion with the fluid within the reservoir resulting in an attrac-

tion toward the needles as the device came into close contact (**Figure 5A**). Once removed, no build-up of fluid was observed due to a reduced surface tension between the liquid and solid. In contrast, untreated hollow microneedles did not attract the fluid within the reservoir when in close contact and once removed the fluid was observed to “stick,” surrounding the needles but not flowing through the bore, due to the higher surface tension between the liquid and solid on the hydrophobic surface (**Figure 5B**).

As presented in Video S1 (Supporting Information), to demonstrate uptake and detection, separate $10 \mu\text{g mL}^{-1}$ CRP and 1 ng mL^{-1} PCT spiked solutions were prepared in buffer solutions and placed within individual reservoirs. Although, we have tested detection works at $25 \mu\text{L}$, the tests in the video were conducted using a 12 mL reservoir. Parafilm (with a small hole to allow fluid to access the skin only) and porcine skin was used to simulate a real-life penetration and ensure the spiked solutions could only access the LFAs through the HMN-LFA devices (**Figure 5C**). CRP- and PCT- LFAs were used without device as a positive control (00:00; Video S1, Supporting Information). For HMN-LFA devices, it is important to highlight, as demonstrated in the video, the little force required for the user to penetrate skin with the devices. The samples were left in contact with the spiked solutions for 5 min before imaging the results (**Figure 5D,E**). The hydrophobicity of the untreated hollow microneedle devices resulted in an inability for uptake of the spiked solutions, resulting in no transfer of fluid onto the sample pad and hence no result shown on the LFAs (00:50; Video S1, Supporting Information). However, PEGylated hollow microneedle devices had the ability to uptake and transfer the spiked solution onto the LFA sample pad (02:00; Video S1,

Supporting Information). The test and control line were clearly observed following 5 min, indicating a *positive* result for both CRP and PCT spiked solutions separately at the reported LoD of the LFAs. This is critical as CRP and PCT concentrations above $10\ \mu\text{g mL}^{-1}$ and $1\ \text{ng mL}^{-1}$, respectively, are considered above normal (high) and indicate an inflammatory state, with both potentially increasing to $500\ \mu\text{g mL}^{-1}$ and $10\ \text{ng mL}^{-1}$.^[45–47] With the latter high levels of PCT correlating with severe sepsis.^[46] Highlighting the effectiveness of rapid-diagnostics at this concentration.

Also presented in Video S1 in the Supporting Information (03:05), specially designed double HMN-LFA devices were fabricated as described to enable simultaneous detection of CRP and PCT spiked solution in multi-LFA devices (Figure 5E). Corresponding LFAs were inserted into PEGylated hollow microneedle devices and exposed to a spiked solution containing both $10\ \mu\text{g mL}^{-1}$ CRP and $1\ \text{ng mL}^{-1}$ PCT. After 5 min, the LFAs were imaged as previous. The increased number of needles increases the total volume collected and the two arrays allows for simultaneous detection. After 5 min, two *positive* results were observed indicating successful simultaneous detection of CRP and PCT, respectively. The flexibility of the design allows for tailored alteration of the LFAs to target multiple desired analytes.

Freshly plasma treated hollow microneedle devices exhibited a similar outcome to the PEGylated hollow microneedle devices, however after ≈ 10 days the samples acted like untreated hollow microneedle devices, indicating the reduction in hydrophilicity and nonpermanent effect of the plasma treatment (Figure S13, Supporting Information). This indicates a limited shelf-life for plasma treated devices and further demonstrates the importance of the PEGylation and enhanced shelf life.

3. Conclusion

This study has produced a quick, low-cost, direct manufacturing process for hollow microneedle devices which can be easily incorporated with lateral flow assays to allow for simultaneous detection of multiple inflammation markers. The manufactured 3D-printed hollow microneedles were post-treated using heat/UV treatment and PEGylated to enhance surface chemistry aiding fluid flow and stability. PEGylated hollow microneedles possess prolonged enhanced hydrophilicity enabling sample storage before use. Optimized PEGylated hollow microneedles demonstrated strong mechanical strength and excellent porcine skin penetration ability, giving confidence to skin penetration without failure in application. Following biological evaluation, PEGylated hollow microneedles were considered noncytotoxic to relevant cell lines. Lastly, the hollow microneedle devices had the ability to passively uptake both CRP and PCT simultaneously in a spiked solution and guide the solution onto the sample pad producing two *positive* results, working both as individual tests and as a multidiagnostic devices. This work paves the way for rapid blood-free diagnostics from a low-cost point-of-care device using 3D-printed hollow microneedles.

4. Experimental Section

Materials: Dulbecco's Modified Eagle's medium–high glucose (DMEM) (D6429), C-reactive protein (CRP), polyethylene glycol (PEG),

phosphate buffer saline (PBS) tablets (P4417), polyformaldehyde and hematoxylin and eosin (H&E) were purchased from Sigma-Aldrich (UK). Fetal bovine serum (FBS) (F9665) was acquired from Merck (Germany). Procalcitonin (PCT) and 2-propanol (IPA) $\geq 99.7\%$ was purchased from VWR International (UK). The EZ4U cell proliferation and cytotoxicity assay was obtained from Oxford Biosystems (UK). Excised abdominal pig skin from a single animal was obtained from a local abattoir. Commercially available inflammation marker lateral flow tests were purchased from BioPanda Reagents (Belfast, U.K). High Temperature resin (RS-F2-HTAM-02) was purchased from Formlabs (Formlabs, USA).

Low-Force SLA 3D-Printed Hollow Microneedle Arrays: Computer aided designs (CAD) were developed using AutoCAD (2023, Autodesk, USA) and features 15 hollow microneedles of height 1 mm, base diameter of 1 mm and bore diameter 0.5 mm. The base consists of a 1.5 mm chamfered slit to secure and guide flow onto the sample pad of the LFAs. The CAD file was exported as an .STL file and imported into PreForm (3.22.1 Formlabs, USA). Briefly, the design was tilted to 45° and supports with 0.4 mm touch point size were manually generated to avoid contact with the needles. Following printing (Form 3, Formlabs, USA), the parts were washed in IPA for 20 min using the FormWash (Formlabs, USA) before being heat/UV treated at 80°C for 2 h using the FormCure (Formlabs, USA).

For characterization methods, square samples were printed, and post-treated, in the same manner as above to allow for characterization to be performed (TGA, FTIR and wettability). For viability assays cylindrical samples with $20\ \text{mm}^2$ total surface area were used in accordance with ISO 10993. All other experiments described were with the hollow microneedles. All samples were sterilized using a desktop Prestige Medical Autoclave (Prestige Medical, UK) at 121°C before any experimentation.

PEGylation Surface Modification: Following complete post-treatment the hollow microneedles were plasma treated using a Diener Zepto (Diener, Germany) plasma cleaner. The pressure was firstly reduced to below 0.2 mbar and held for 2 min before introducing oxygen to increase the pressure to 0.7 ± 0.1 mbar for 3 min. After which the generator was switched on for 15 min. Following cleaning the samples were fully submerged in a PEG solution of M_w 10 kDa at 10 wt% for 18 h, as a standard. Following this, the samples were thoroughly rinsed in DI water and left to air dry for 24 h.

Various M_w (0.2, 2, 10, and 20 kDa) and wt% (1, 5, and 10 wt%) were used to investigate the effect on the prolonged wettability of the resultant prints.

Assembly of Hollow Microneedle-Lateral Flow Assay Device: Once required the hollow microneedles were sterilized. Meanwhile, LFAs were removed from the packaging and the LFA was removed from the cassette. The sample pad was inserted into the slit until fully inserted. The HMN-LFA devices were used immediately, as per the instructions of the LFAs.

Characterization Methods: Thermal properties of the 3D prints were evaluated with thermogravimetric analysis (TGA). The tests were performed in an inert atmosphere using the Setsys Evolution TGA 16/18 (Setaram, France). Dynamic scans were performed at a heating rate of $10^\circ\text{C min}^{-1}$ from room temperature up to 800°C .

Fourier-transform infrared spectroscopy (FTIR) was obtained using the iD5 attenuated total reflectance (ATR)-mode of a Nicolet iS5 FTIR spectrometer (Thermo Fisher Scientific, USA). Each spectrum represents the average of 126 scans in the wavelength range of $4500 - 600\ \text{cm}^{-1}$ with a spectral resolution of $1\ \text{cm}^{-1}$.

The wettability was assessed using an optical contact angle goniometer, OCA 25 (Data Physics, UK) at ambient temperature. A $0.5\ \mu\text{L}$ DI water droplet was dispensed at the surface of each sample and allowed to settle for 10 s. Contact angle calculations were performed on the accompanying software. The process was repeated over a prolonged period of time, totaling 30 days. Following testing, the samples were left to air dry and stored at room temperature until future testing. These tests were repeated three times per specimen, for three hollow microneedle specimens, $n = 9$ in total.

Atomic force microscopy (Jupiter XR, Oxford Instruments) was used to evaluate surface topography and to quantify roughness of control, plasma treated and PEGylated samples. Measurements were carried out

in blueDrive Tapping Mode, with AC160TS-R3 tips. A total of 20 areas of $10 \times 10 \mu\text{m}$ were imaged per sample, $n = 20$. Analysis of RMS surface roughness' was performed on Gwyddion using the statistical quantities tool.

All optical microscopy was performed using the Keyence VHX 6000 (Milton Keynes, UK) with the variable up to 200 \times lens attached. Images were taken at 0 $^\circ$ or 50 $^\circ$ using depth composition and 3D mode.

Mechanical Testing: The mechanical strength of sterilized hollow microneedles were tested using a Mettler Toledo DMA1 (Mettler Toledo, USA) dynamic mechanical analyzer (DMA). The hollow microneedle samples were attached to a bottom titanium plate, while the top titanium plate was lowered until contact was made with the hollow microneedle tip, indicated by a recorded force on the DMA screen. A compressive force from the bottom plate was applied from 0 to 2 N at a rate of 0.25 N min $^{-1}$, while the resultant displacement was recorded. The samples were imaged using optical microscopy following testing to determine the resultant damage. These tests were repeated for three untreated-, three UV/Heat treated- and three PEGylated- hollow microneedle specimens, $n = 3$ in total.

Penetration of Porcine Skin: Excised porcine skin was obtained from a local abattoir. Normal high temperature cleaning procedures were not used to preserve the integrity of the skin barrier. Within 24 h of slaughter, the porcine skin was washed with water, sliced with a dermatome to a nominal thickness of 750 μm and frozen. Before use, the frozen skin was thawed and cut down to $\approx 2 \text{ cm}^2$ and placed on a supporting structure. The sterilized hollow microneedles were inverted and placed on top of the skin. Using a known mass, a force equating to roughly 1.5 N was applied and maintained for 1 minute before removing. The resultant pores were analyzed using optical microscopy. The % penetration was calculated by assessing the percentage of needles penetrated (N_p) against the total number of needles (N_T) (Equation (3))

$$\% \text{ Penetration} = \frac{N_p}{N_T} \times 100 \quad (3)$$

Histological analysis was performed by pressing the hollow microneedles into porcine skin using thumb pressure for 1 minute before being submerged in a 4% PFA solution overnight. The skin samples were dehydrated using increasing concentrations of ethanol before being embedded in paraffin and sectioned into 7 μm thick slices using a microtome (Leica HistoCore, BIOCUT) and stained with hematoxylin and eosin (H&E). The stained skin samples were examined using an inverted microscope (EVOS M5000, Invitrogen, USA).

To assess mechanical properties of the hollow microneedles while penetrating skin, porcine skin was attached to the bottom plate of the DMA, with hollow microneedles attached to the upper plate. The hollow microneedles were brought into contact with the porcine skin as indicated by a recorded force on the DMA screen, and a compressive force was applied from 0 to 2 N at a rate of 0.25 N min $^{-1}$. These tests were repeated for three PEGylated hollow microneedle specimens, $n = 3$ in total.

Additionally, to assess forces exerted during skin penetration, an Electropuls E10000 linear-torsion dynamic material test machine (Instron, USA) with 1 kN load cell was used. A laser engineered buffer table was used to prevent damage to the equipment, parafilm was placed on top of the buffer table to avoid damage to the hollow microneedles due to the buffer table, lastly porcine skin was placed on top of the parafilm. The hollow microneedles were attached to the upper plate. The hollow microneedles were manually brought into contact with the porcine skin, a 4 N force was applied over 30 s to ensure skin penetration, the hollow microneedles were then lowered to 0.75 mm into the skin over 2 min, before being held in the skin for 60 s, with force and displacement recorded throughout (WaveMatrix2, Instron, USA). These tests were repeated for three further hollow microneedle specimens, $n = 4$ in total.

Biological Evaluation: Human dermal adult fibroblasts (HuDAF) and human keratinocytes (strain Km) were generously provided by the Walko lab, from stocks originally obtained from the Watt laboratory.^[48] Human breast cancer cells MDA-MB-231 cells were from Jungwirth laboratory stocks originally obtained from the Isacke laboratory.^[49] All cells were routinely subject to mycoplasma testing. All cells were cultured at 37 $^\circ\text{C}$ and

5% CO $_2$ and were passaged at $\approx 80\%$ confluence. All cells were cultured in DMEM supplemented with 10% FBS, 1% penicillin/streptomycin and $2 \times 10^{-3} \text{ M}$ L-glutamine.

In case of colony formation and viability assays, hollow microneedles or cylindrical (20 mm 2 surface area) devices were used, respectively. Plasma-treated and PEGylated devices were added directly to cultured cells. To test the effects of leachable substances from the devices, cell culture medium was incubated with the devices for 24 h at 37 $^\circ\text{C}$ (0.5 mL per cylindrical device for viability, 1 mL per hollow microneedle device for colony formation). This culture media was then added directly to the cells. As a positive control for cytotoxic effects, uncured resin was incubated with cell culture media (1/4 v/v) for 24 h and added directly to cells.

For viability assays, 2×10^4 cells well $^{-1}$ were seeded into 24-well plates. After 24 h, cells were exposed to one hollow microneedle device, culture media, or control conditions. 24 h post-treatment, cell viability was measured using the EZ4U Cell Proliferation and Cytotoxicity Assay kit (Oxford biosystem, B1-5000) according to the manufacturer's instructions. In brief, 100 μL of 1:10 diluted EZ4U substrate were added per well and plates incubated at 37 $^\circ\text{C}$ for 1.5 h. The supernatant was transferred to a flat bottom 96-well plate to measure the absorbance (450 nm) using a BMG FLUOstar Omega plate reader. Viability values were normalized to viability of untreated control cells.

For colony formation assays, 100 cells well $^{-1}$ were seeded into 6-well plates. After 24 h, the cells were exposed to the hollow microneedle devices or controls. Cell colonies were stained 7 days later with crystal violet (Fisher Scientific, 10646972, 0.5% w/v crystal violet in 25% v/v methanol/water). Plates were imaged using a flatbed scanner and colonies counted.

Multianalyte-multi-LFA detection: A stock 100 $\mu\text{g mL}^{-1}$ CRP solution was prepared by diluting 100 μL of 10 $\mu\text{g mL}^{-1}$ CRP solution to 10 mL using a standard PBS solution and stored until required. Once required a sufficient volume of 10 $\mu\text{g mL}^{-1}$ CRP solution was made up by diluting the stock in standard PBS solution. A stock 10 $\mu\text{g mL}^{-1}$ PCT solution was prepared by diluting 10 μg of PCT into 1 mL of PBS solution. Once required sufficient volume of 1 ng mL $^{-1}$ PCT solution was prepared. A CRP/PCT mixed solution was prepared by combining equal volumes of spiked 20 $\mu\text{g mL}^{-1}$ CRP and 2 ng mL $^{-1}$ PCT solutions, which resulted in a final spiked solution of 10 $\mu\text{g mL}^{-1}$ CRP and 1 ng mL $^{-1}$ PCT solution.

Fully combined HMN-LFA devices were penetrated through parafilm so only the needles exposed. The devices were lowered into the spiked solutions until contact with the fluid was made. The device was held in this position for 5 min before being blot dried to remove excess fluid. Following this, the LFAs were observed for the results as the test and control lines. Control, plasma treated, and PEGylated hollow microneedles were used in comparison.

Statistical Analysis: Statistical analysis between various samples was performed using paired sample Student's two tail t-test, where n.s.; not significant is indicated by a p -value greater than 0.05. Statistical analysis of biological evaluation data was performed using one-way ANOVA with Tukey's post hoc test, where n.s.; not significant is indicated by a p -value greater than 0.05. All statistical analyses were performed using Excel Data Analysis Tools (Microsoft, USA).

Supporting Information

Supporting Information is available from the Wiley Online Library or from the author.

Acknowledgements

J.G.T. and H.S.L. thank Abbott Diabetes Care Ltd. and EPSRC EP/R513155/1 for their funding support. H.S.L. acknowledges the EPSRC EP/V010859/1, EP/V051083/1 and the Royal Society Research Grant RSG\R1\201185 for their support. The authors thank Prof Richard Guy for the important discussions and donation of porcine skin. The authors thank the Department of Chemistry at the University of Bath

for allowing us the use of equipment in their facility. The authors acknowledge the reviewers contributions through their feedback during review.

Conflict of Interest

The authors declare no conflict of interest.

Data Availability Statement

The data that support the findings of this study are openly available in Dataset for “3D Printed Hollow Microneedle-Lateral Flow Devices for Rapid Blood-free Diagnostics” at <https://researchdata.bath.ac.uk/1233/>.

Keywords

3D printing, biocompatibility, hollow microneedles, inflammation markers, rapid diagnostics, skin penetration

Received: February 19, 2023

Revised: March 30, 2023

Published online: May 4, 2023

- [1] S. Sakamoto, W. Putalun, S. Vimolmangkang, W. Phoolcharoen, Y. Shoyama, H. Tanaka, S. Morimoto, *J. Nat. Med.* **2018**, *2018*.
- [2] I. A. Mattioli, A. Hassan, O. N. Oliveira Jr, F. N. Crespilho, *ACS Sens.* **2020**, *5*, 3655.
- [3] J. S. Nouetchognou, J. Ateudjieu, B. Jemea, D. Mbanja, *BMC Res. Notes* **2016**, *9*.
- [4] J. G. Hamilton, *J. Fam. Pract.* **1995**, *41*.
- [5] J. Rashid, O. Taiwo, I. Ahluwalia, S. Chungong, *Emerging Infect. Dis. J.* **2004**, *10*.
- [6] K. M. Koczula, A. Gallotta, *Essays Biochem.* **2016**, *60*.
- [7] J. Parkin, B. Cohen, *Lancet* **2001**, *357*, 1777.
- [8] B. R. Bistran, *Crit. Care Med.* **1999**, *27*, 452.
- [9] J.-A. Ryu, J. H. Yang, D. Lee, C.-M. Park, G. Y. Suh, K. Jeon, J. Cho, S. Y. Baek, K. C. Carriere, C. R. Chung, *PLoS One* **2015**, *10*, e0138150.
- [10] P. Schuetz, A. Beishuizen, M. Broyles, R. Ferrer, G. Gavazzi, E. H. Gluck, J. González Del Castillo, J. U. Jensen, P. L. Kanizsai, A. L. H. Kwa, S. Krueger, C. E. Luyt, M. Oppert, M. Plebani, S. A. Shlyapnikov, G. Toccafondi, J. Townsend, T. Welte, K. Saeed, *Clin. Chem. Lab. Med.* **2019**, *57*, 1308.
- [11] M. L. Brigden, *Am. Fam. Physician* **1999**, *60*.
- [12] A. Osei-Bimpong, J. Meek, S. Lewis, *Hematology* **2007**, *12*, 353.
- [13] K. Chiscaden, World Health Organization, <https://www.who.int/news/item/08-09-2020-who-calls-for-global-action-on-sepsis—cause-of-1-in-5-deaths-worldwide> (accessed: January 2022).
- [14] K. E. Rudd, S. C. Johnson, K. M. Agesa, K. A. Shackelford, D. Tsoi, D. R. Kievlan, D. V. Colombara, K. S. Ikuta, N. Kissoon, S. Finfer, *Lancet* **2020**, *395*, 200.
- [15] C. Fleischmann, F. Reichert, A. Cassini, R. Horner, T. Harder, R. Markwart, M. Tröndle, Y. Savova, N. Kissoon, P. Schlattmann, *Arch. Dis. Child.* **2021**, *106*, 745.
- [16] C. Pierrakos, J.-L. Vincent, *Crit. Care* **2010**, *14*, R15.
- [17] C. Lelubre, S. Anselin, K. Zouaoui Boudjeltia, P. Biston, M. Piagnerelli, *Biomed Res. Int.* **2013**, *2013*, 124021.
- [18] V. Kolb-Bachofen, *Immunobiology* **1991**, *183*, 133.
- [19] U. Sjöbom, K. Christenson, A. Hellström, A. K. Nilsson, *Front Immunol* **2020**, *11*.
- [20] J. G. Turner, L. R. White, P. Estrela, H. S. Leese, *Macromol. Biosci.* **2021**, *21*, 2000307.
- [21] M. R. Prausnitz, *Adv. Drug Delivery Rev.* **2004**, *56*, 581.
- [22] P. R. Miller, R. M. Taylor, B. Q. Tran, G. Boyd, T. Glaros, V. H. Chavez, R. Krishnakumar, A. Sinha, K. Poorey, K. P. Williams, *Commun Biol* **2018**, *1*, 173.
- [23] T. Wu, X. You, Z. Chen, *Sensors* **2022**, *22*.
- [24] M. Gerstel, V. Place, Drug Delivery Device, Patent **1971**.
- [25] P. M. Wang, M. Cornwell, M. R. Prausnitz, *Diabetes Technol. Ther.* **2005**, *7*.
- [26] X. Jiang, P. B. Lillehoj, *Microsyst. Nanoeng.* **2020**, *6*.
- [27] C. J. Bolton, O. Howells, G. J. Blayney, P. F. Eng, J. C. Birchall, B. Gualeni, K. Roberts, H. Ashraf, O. J. Guy, *Lab Chip* **2020**, *20*, 2788.
- [28] J. Tu, N. Reeves, *Open Eng.* **2019**, *9*, 167.
- [29] C. Yeung, S. Chen, B. King, H. Lin, K. King, F. Akhtar, G. Diaz, B. Wang, J. Zhu, W. Sun, *Biomicrofluidics* **2019**, *13*, 064125.
- [30] International Organization for Standardization, Biological evaluation of medical devices, <https://www.iso.org/standard/68936.html> **2018** (accessed: November 2022).
- [31] C. Hart, C. M. Didier, F. Sommerhage, S. Rajaraman, *Biosensors* **2020**, *10*, 152.
- [32] Formlabs. Using High Temp Resin, https://support.formlabs.com/s/article/Using-High-Temp-Resin?language=en_US (accessed: January 2022).
- [33] H. S. Gill, D. D. Denson, B. A. Burris, M. R. Prausnitz, *Clin. J. Pain* **2008**, *24*, 585.
- [34] M. U. Ahmed, M. M. Hossain, M. Safavieh, Y. L. Wong, I. A. Rahman, M. Zourob, E. Tamiya, *Crit. Rev. Biotechnol.* **2016**, *36*.
- [35] T. W. Bacha, D. C. Manuguerra, R. A. Marano, J. F. Stanzione, *RSC Adv.* **2021**, *11*, 21745.
- [36] D. Bodas, C. Khan-Malek, *Sens. Actuators, B* **2007**, *123*, 368.
- [37] Y. Yokoyama, S.-i. Yusa, *Polym. J.* **2013**, *45*, 985.
- [38] V. Sharma, D. S. Patel, V. Jain, J. Ramkumar, *Int. J. Mach. Tools Manuf.* **2020**, *155*, 103579.
- [39] V. Luque-Agudo, M. Hierro-Oliva, A. M. Gallardo-Moreno, M. L. González-Martín, *Polym. Test.* **2021**, *96*, 107097.
- [40] S. P. Davis, B. J. Landis, Z. H. Adams, M. G. Allen, M. R. Prausnitz, *J. Biomech.* **2004**, *37*, 1155.
- [41] J. H. Park, M. R. Prausnitz, *J. Korean Phys. Soc.* **2010**, *56*.
- [42] A. Summerfield, F. Meurens, M. E. Ricklin, *Mol. Immunol.* **2015**, *66*, 14.
- [43] L. K. Branski, R. Mittermayr, D. N. Herndon, W. B. Norbury, O. E. Masters, M. Hofmann, D. L. Taber, H. Redl, M. G. Jeschke, *Burns* **2008**, *34*, 1119.
- [44] R. Gref, A. Domb, P. Quellec, T. Blunk, R. Müller, J.-M. Verbavatz, R. Langer, *Adv. Drug Delivery Rev.* **1995**, *16*, 215.
- [45] A. Binnie, J. Lage, C. C. Dos Santos, in *Evidence-Based Practice of Critical Care*, 3rd ed. (Eds: C. S. Deutschman, et al.), Elsevier, Amsterdam **2020**, p. 319.
- [46] M. Meisner, *Ann. Lab. Med.* **2014**, *34*, 263.
- [47] Mayo Clinic. ‘C-reactive protein test’, <https://www.mayoclinic.org/tests-procedures/c-reactive-protein-test/about/pac-20385228#:~:text=CRP%20is%20measured%20in%20milligrams> (accessed: November 2021 and November 2022).
- [48] G. Walko, S. Woodhouse, A. O. Pisco, E. Rognoni, K. Liakath-Ali, B. M. Lichtenberger, A. Mishra, S. B. Telerman, P. Viswanathan, M. Logtenberg, L. M. Renz, G. Donati, S. R. Quist, F. M. Watt, *Nat. Commun.* **2017**, *8*.
- [49] U. Jungwirth, A. van Weverwijk, R. J. Evans, L. Jenkins, D. Vicente, J. Alexander, Q. Gao, S. Haider, M. Iravani, C. M. Isacke, *Nat. Commun.* **2021**, *12*.